Michael R. Kaus, PhD
Simon K. Warfield, PhD
Arya Nabavi, MD
Peter M. Black, MD, PhD
Ferenc A. Jolesz, MD
Ron Kikinis, MD

Index terms:
Brain neoplasms, 10.363, 10.366
Brain neoplasms, MR, 10.121412, 10.12143
Magnetic resonance (MR), technology
Magnetic resonance (MR), three-dimensional, 10.121412, 10.12143
Magnetic resonance (MR), volume measurement, 10.121412, 10.12143
Technology assessment

Radiology 2001; 218:586–591

Abbreviations:
ICC = intracranial cavity
3D = three-dimensional
2D = two-dimensional

[1] From the Surgical Planning Laboratory, Depts of Radiology (M.R.K., S.K.W., A.N., F.A.J., R.K.) and Neurosurgery (A.N., P.M.B.), Brigham and Women's Hospital, Harvard Medical School, 75 Francis St, Boston, MA 02115; and Lehrstuhl Technische Elektronik, University Erlangen-Nürnberg, Erlangen, Germany (M.R.K.). Received Dec 30, 1999; revision requested Feb 21, 2000; revision received and accepted May 5. Supported in part by Deutscher Akademischer Austauschdienst D/96/34017 (M.R.K.); National Multiple Sclerosis Society grant (S.K.W.); NIH grants P01 CA67165 (R.K., F.A.J.), 1R01RR11747 (R.K.), 1P41RR13218 (R.K., F.A.J., S.K.W.); and Deutsche Forschungsgemeinschaft HA 359/1-1 (A.N.). **Address correspondence to** R.K. (e-mail: *kikinis@bwh.harvard.edu*).

Author contributions:
Guarantors of integrity of entire study, all authors; study concepts, all authors; study design, M.R.K., A.N., S.K.W., R.K.; definition of intellectual content, all authors; literature research, M.R.K.; clinical studies, A.N., P.M.B.; data acquisition, M.R.K., A.N.; data analysis, M.R.K.; statistical analysis, M.R.K., S.K.W.; manuscript preparation, M.R.K.; manuscript editing, M.R.K.; manuscript review, all authors.

Automated Segmentation of MR Images of Brain Tumors[1]

An automated brain tumor segmentation method was developed and validated against manual segmentation with three-dimensional magnetic resonance images in 20 patients with meningiomas and low-grade gliomas. The automated method (operator time, 5–10 minutes) allowed rapid identification of brain and tumor tissue with an accuracy and reproducibility comparable to those of manual segmentation (operator time, 3–5 hours), making automated segmentation practical for low-grade gliomas and meningiomas.

Computer-assisted surgical planning and advanced image-guided technology have become increasingly used in neurosurgery (1–5). The availability of accurate anatomic three-dimensional (3D) models substantially improves spatial information concerning the relationships of critical structures (eg, functionally significant cortical areas, vascular structures) and disease (3,4,6). In daily clinical practice, however, commercially available intraoperative navigational systems provide the surgeon with only two-dimensional (2D) cross sections of the intensity-value images and a 3D model of the skin. The main limiting factor in the routine use of 3D models to identify (segment) important structures is the amount of time and effort that a trained operator must spend on the preparation of the data (3,6). The development of automated segmentation methods has the potential substantially reduce the time for this process and to make such methods practical.

Although 2D images accurately depict the size and location of anatomic objects, the process of generating 3D views to visualize structural information and spatial anatomic relationships is a difficult task, which is usually carried out in the clinician's mind. Image-processing tools provide the surgeon with interactively displayed 3D visual information that is somewhat similar to the view of the surgeon during surgery; the use of these tools facilitates comprehension of the entire anatomy. For example, the (mental) 3D visualization of structures that do not readily align with the planes of the images (eg, the vascular tree) is difficult if it is based on 2D images alone.

Image-based modeling requires the use of computerized image-processing methods, which include segmentation, registration, and display. Segmentation with statistical classification techniques (7,8) has been successfully applied to gross tissue type identification. Because the acquisition of tissue parameters is insufficient for successful segmentation due to the lack of contrast between normal and pathologic tissue (9,10), statistical classification may not allow differentiation between nonenhancing tumor and normal tissue (11–13). Explicit anatomic information derived from a digital atlas has been used to identify normal anatomic structures (14–16).

We developed an automated segmentation tool that can be used to identify the skin surface, ventricles, brain, and tumor in patients with brain neoplasms (17,18). The purpose of the current study was to compare the accuracy and reproducibility of this automated method with those of manual segmentation carried out by trained personnel.

Materials and Methods

Imaging Protocol

The heads of patients were imaged in the sagittal and transverse planes with a 1.5-T magnetic resonance (MR) imaging system (Signa; GE Medical Systems, Milwaukee, Wis) and a contrast material–enhanced 3D sagittal spoiled gradient-recalled acquisition with contiguous sections (flip angle, 45°; repetition time msec/echo time msec, 35/7; field of view, 240 mm; section thickness, 1.5 mm; matrix, 256 × 256 × 124). The acquired MR images were transferred to a Unix network via an Ethernet connection.

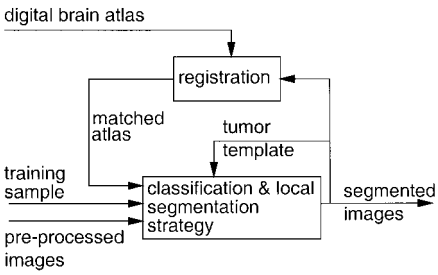

Figure 1. Diagram of the tumor segmentation scheme.

Brain Tumor Patients

Twenty patients were selected from a neurosurgical database of images in approximately 260 patients with brain tumors. Cases of the 260 patients had been postprocessed for image-guided neurosurgery by using a combination of semiautomated techniques and manual outlining of the skin surface, brain, ventricles, vessels, and tumor.

Two neurosurgeons (including A.N.) were asked to select 20 cases with meningiomas and low-grade gliomas of different sizes, shapes, and locations to provide a representative selection. These two types were selected because they are relatively homogeneous and have well-defined imaging characteristics. Pathologic diagnoses included six meningiomas (cases 1–3, 11, 12, 16), and 14 low-grade gliomas (cases 4–10, 13–15, 17–20). In this study, six of six meningiomas were well enhancing, and 14 of 14 low-grade gliomas were nonenhancing.

Cases 1–10 formed the development database used for the design and validation of the automated segmentation method. To ensure that the method produced correct results when applied to cases other than those of the development database, validation was carried out separately with the validation data sets from cases 11–20 in addition to validation with the 10 development cases.

Automated Segmentation of Brain and Tumor

General segmentation framework.—We adopted a general algorithm called adaptive template–moderated classification (see references 17 and 18 and the Appendix for details). The technique involves the iteration of statistical classification to assign labels to tissue types and nonlinear registration to align (register) a digital anatomic atlas (presegmented anatomic map) to the patient data (Fig 1). Statistical classification was used to divide an image into different tissue classes on the basis of the signal intensity value. If different tissue classes have the same or overlapping grey-value distributions (eg, cerebrospinal fluid and fluid within the eyeballs), such methods fail. Therefore, additional information about the spatial location of anatomic structures was derived from a registered anatomic atlas (manually segmented MR image of a single subject) (6). Objects of interest were identified on the classified images with local segmentation operations (mathematic morphology and region growing) (19).

Application to tumor segmentation.—For the task of brain tumor segmentation, the order in which the structures of interest were segmented followed a simple hierarchical model of anatomy (Fig 2). By proceeding hierarchically from the outside to the inside of the head, each segmented structure defined a refined region of interest for the next structure to be segmented. Five different tissue classes were modeled: background, skin (fat and bone), brain, ventricles, and tumor. Because of the homogeneous tissue composition of meningiomas and low-grade gliomas, one tissue class was sufficient for the statistical model.

An atlas of normal anatomy does not include pathologic structures. As a result, templates from the atlas were derived for only the head, brain, and ventricles. First, the whole head was segmented from the background by using thresholding and local segmentation strategies. On the basis of the segmentation of the head, an initial alignment of the atlas to the patient was established. Next, the intracranial cavity (ICC) was segmented from the head in two segmentation iterations (statistical classification, local segmentation strategy, and reregistration of the atlas).

At this point, all voxels belonging to the brain, ventricles, and tumor were labeled as ICC. In the first iteration, the ICC was segmented by using the head and ICC template from the initially registered atlas. The atlas was then realigned on the basis of the whole head and ICC of the patient. This step was followed by a second classification and local segmentation step. The ventricles were segmented from the ICC in a third segmentation iteration. At this point, the ICC contained only voxels belonging to the brain and tumor.

Having defined a region of interest for the tumor, which was located inside the brain and outside the ventricles and skin (fat and bone), the tumor was segmented in two iteration cycles. In the first iteration, the tumor was classified by using the anatomic knowledge from only the atlas; this step was followed by application of the local segmentation strategy. Because there was no tumor template in the atlas, a straightforward registration was not possible. Consequently, tumor voxels were relabeled as ICC voxels prior to the registration process. As a result, a spatial correspondence between the atlas and patient data set was established for every voxel, since the patient data set contained no voxels labeled as tumor at the time registration of the atlas was carried out.

In the second iteration, tumor segmentation from the first iteration was used as an anatomic template. Although this template was approximate, the additional information about the location of the tumor prevented misclassification of voxels distant to the atlas template as tumor.

Initialization of the automated segmentation method.—To reduce noise on the MR image without blurring object edges, an anisotropic diffusion–filtering method was applied (20). For the initialization of the automated segmentation method, a graphical user interface was developed for the 2D display of MR imaging sections and the selection of example tissue points with use of a mouse (Fig 3). The only interaction required by the operator (see Validation Experiments) was the selection of three to four example points for each tissue class, that is, skin (fat and bone), brain, ventricles, and tumor. The program calculated a statistical model for the distribution of the gray values on the basis of these manually selected tissue prototypes.

Manual Segmentation of Brain and Brain Tumor

For manual segmentation of the brain and tumor, an interactive segmentation tool was used (MRX; GE Medical Systems) on an Ultra 10 workstation (Sun Microsystems, Mountain View, Calif). Human operators outlined the structures section by section (see Validation Experiments) by pointing and clicking with a mouse. The program connected consecutive points with lines. An anatomic object was defined by a closed contour, and the program labeled every voxel of the enclosed volume.

Validation Experiments

Because of the lack of an acceptable standard (eg, realistic phantom) for comparison, our definition of a segmentation standard was based on the manual segmentations with interactive computer

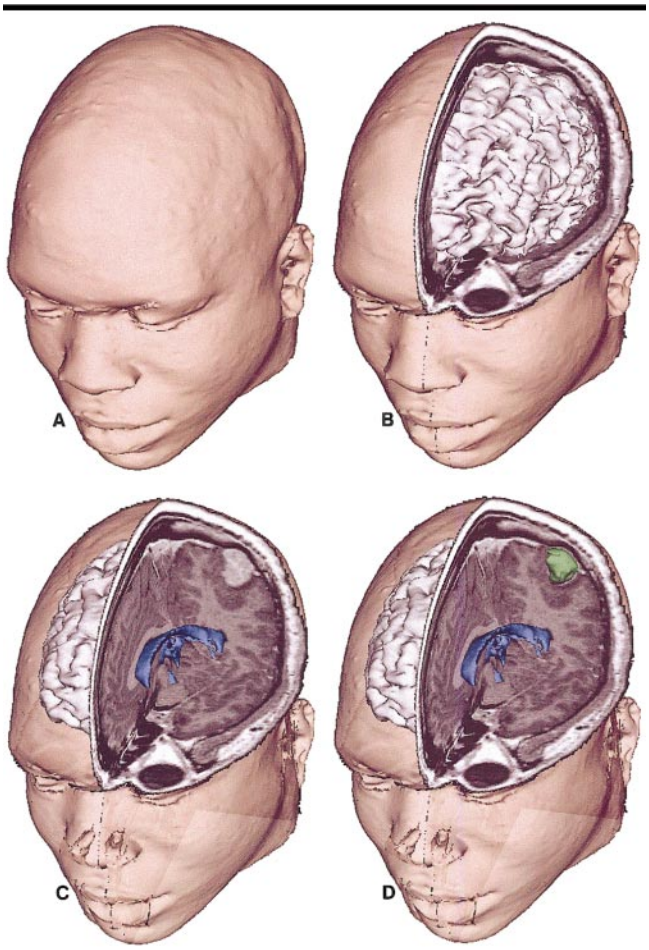

Figure 2. Diagram of the hierarchical segmentation method, which proceeds from *A* to *D*.

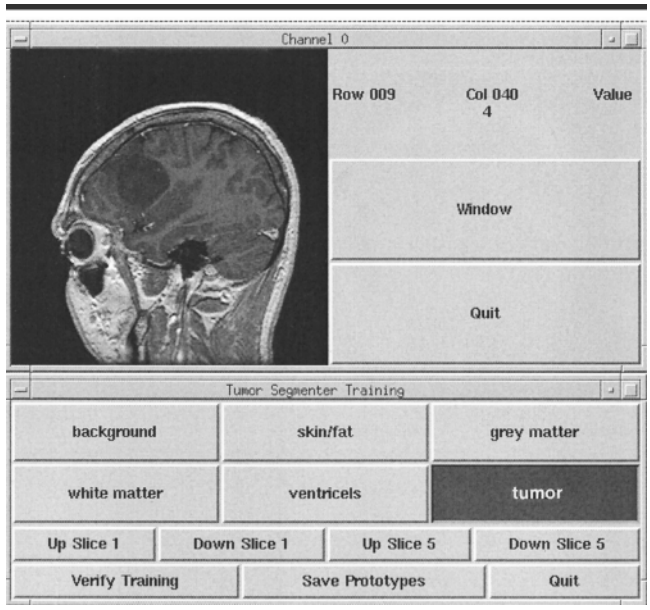

Figure 3. Graphical user interface for the automated segmentation method to allow the 2D display of MR sections and the selection of example tissue points with a mouse.

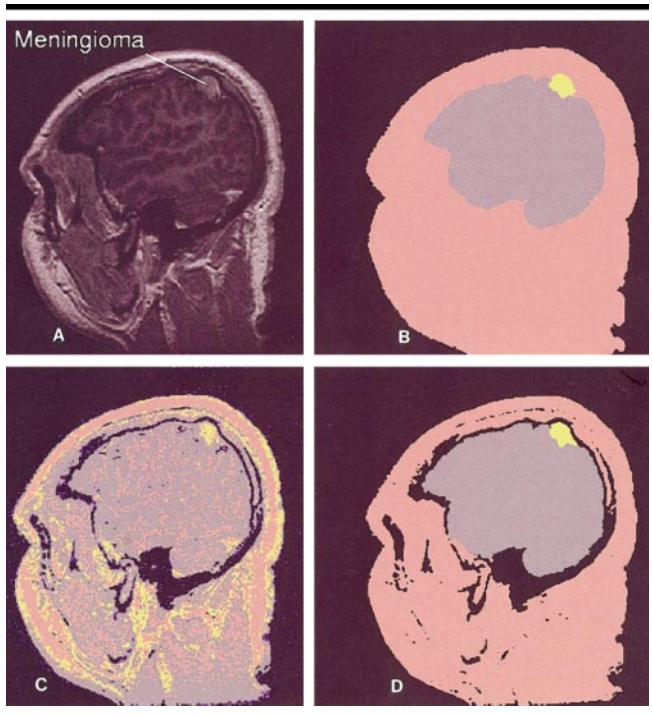

Figure 4. Example of a spoiled gradient-recalled image. *A*, Meningioma. *B*, Manual segmentation, *C*, Statistical classification. *D*, Template-moderated segmentation.

segmentation tools. However, manual segmentation is subject to interobserver variability and human error (6). To minimize the influence of these factors while maintaining a means of measuring the segmentation accuracy of the individual raters, the standard was defined on the basis of the segmentations of four independent human observers. A single 2D section was randomly selected from the subset of the MR imaging volume that showed the tumor. The four human observers then independently outlined the brain and tumor on this section by hand. The standard segmentation of brain and tumor in each patient data set was defined as the area of those voxels in which at least three of four raters agreed regarding their identification. All other voxels were labeled as background.

To assess accuracy, the automated segmentation tool was trained once with a single MR imaging section containing all tissue types of interest and was executed on the full 3D data set. This process resulted in segmentation of the entire data set. For each data set, the structures skin (fat and bone), brain, ventricles, and tumor were segmented.

The interrater variability of the four independent manual and the four independent automated segmentations was measured on the basis of all 20 cases. For the measurement of intraobserver variability, one of the medical experts also manually segmented the selected 2D section four times during 1 week in each of the 20 cases. Training of the automated method was also carried out four times during 1 week in all 20 cases.

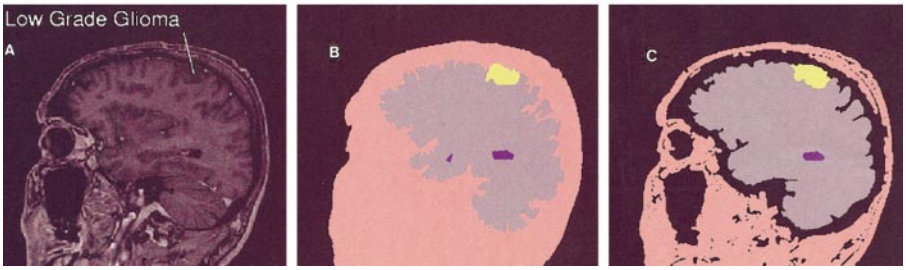

Figure 5. Example of manual and automated segmentation of a low-grade glioma. *A*, On a spoiled gradient-recalled image. *B*, With manual segmentation. *C*, With template-moderated segmentation.

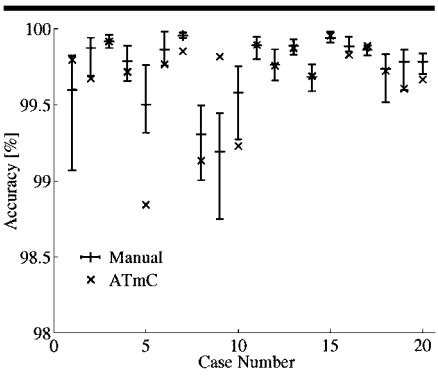

Figure 6. Brain segmentation accuracy of the manual (mean, minimum, and maximum) and automated methods (*ATmC*) in the 20 brain tumor cases (meningioma cases, 1–3, 11, 12, 16; low-grade glioma cases, 7–10, 13–15, 17–20). Accuracy with the automated method was consistent with that of manual segmentation in most cases.

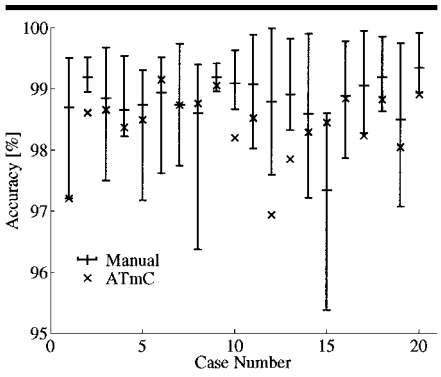

Figure 7. Tumor segmentation accuracy of the manual (mean, minimum, and maximum) and automated methods (*ATmC*) in the 20 brain tumor cases (meningioma cases, 1–3, 11, 12, 16; low-grade glioma cases, 7–10, 13–15, 17–20). Accuracy with the automated method was consistent with that of manual segmentation in most cases.

Intra- and Interobserver Variability for All 20 Cases

Segmented Volume and Tumor Histologic Type	Manual Method		Automated Method	
	Intraobserver	Interobserver	Intraobserver	Interobserver
Brain				
Meningioma	0.42 ± 0.03	4.93 ± 1.75	0.36 ± 0.45	1.84 ± 0.65
Low-grade glioma	1.79 ± 1.53	6.31 ± 2.85	1.44 ± 1.33	2.71 ± 1.68
Tumor				
Meningioma	1.58 ± 0.98	7.08 ± 2.18	0.66 ± 0.72	2.66 ± 0.38
Low-grade glioma	2.08 ± 0.78	13.61 ± 2.21	2.06 ± 1.73	2.97 ± 1.58

Note.—Data are the mean coefficient of variation percentage plus or minus the SD.

During all experiments, the times for manual outlining, training, and computation for the automated segmentation method were recorded.

Statistical Analysis

Qualitative analysis was carried out on the basis of volume-of-overlap comparison with standard (accuracy) and overall volume variability (reproducibility) in the 2D section selected. Segmentation accuracy was defined as the percentage of correctly classified voxels (in object and background) with respect to the total number of voxels V on the image, that is, $(TP + TN)/V$, where TP is the number of true-positive voxels and TN is the number of true-negative voxels (21). The mean and SDs of the accuracy values with respect to the 20 test cases were also calculated (Matlab version 4.1; Mathworks, Cambridge, Mass).

To assess the inter- and intrarater variability error, the coefficient of variation CV% was calculated as follows: $CV\% = 100(SD_{volume}/Mean_{volume})$. The coefficient of variation does not measure the correctness of segmentation, only the change in the volume of objects in segmentations of different raters.

Results

Examples of manual and automated segmentation of a meningioma (Fig 4) and low-grade glioma (Fig 5) indicate the similarity between the results with the two methods.

Segmentation accuracy with the automated method was high and within the range of accuracy of the manual method. The overall mean accuracy for tumor segmentation for all 20 cases was 99.68% ± 0.29% (SD) with the automated method and 99.68% ± 0.24% with the manual method (Fig 6), while the mean accuracy for brain segmentation for all 20 cases was 98.40% ± 0.57% and 98.81% ± 0.88%, respectively (Fig 7).

Intraobserver variability (coefficients of variation) for both the automated and manual methods was low. For brain and tumor segmentation, mean intraobserver variability for all 20 cases with the automated method was 0.10%–3.57% and 0.14%–4.70%, while the manual method had coefficient of variation values of 0.24%–4.11% and 0.80%–3.28% (Table).

Interobserver variability was lower with the automated method than with the manual method. Mean interobserver variability for all 20 cases with the automated method was 0.33%–4.72% and 0.99%–6.11% for brain and tumor segmentation, respectively, while the manual method achieved coefficient of variation values of 2.62%–10.51% and 3.58%–14.42% (Table).

Automated segmentation of a complete 3D image volume required approximately 75 minutes of unsupervised computation time (Sun ES 6000 server, 20 central processing units with 250-MHz speed and 5 Gbyte of random-access memory; Sun Microsystems). The overall operator time for training of the automated method was approximately 5–10 minutes (selection of example voxels for each of the relevant tissue classes). Manual outlining of brain and tumor required 1–3 minutes per section. Time for manual segmentation of the 3D volume was on the order of 3–5 hours.

Discussion

Our findings show that brain, meningiomas, and low-grade gliomas can be

accurately and reproducibly segmented by means of automated processing of gradient-echo MR images. We have shown that our algorithm allows complete segmentation of the brain and tumor and requires only the manual selection of a small sample of example voxels (21–28 voxels).

The goals of the development of automated segmentation tools are to make segmentation of MR images more practical by replacing manual outlining, which reduces operator time, without a measurable effect on the results and to improve reproducibility. However, the validity of our segmentations is difficult to assess without the availability of a standard. Therefore, our validation study was designed to determine how closely the raters agreed within a single method (automated and manual) and how closely the segmentation results correlated between the two methods.

Segmentation accuracy with the automated method was high and within (maximum difference, 0.6%) the accuracy range of the manual method. The errors with automated brain segmentation were in part due to over- and undersegmentation in the area of the tentorium and the lateral sulcus with abundant vessels. The algorithm tended to cause oversegmentation in these areas if parts of the neck near the cerebellum were misclassified as brain and if the ICC template derived from the atlas was misaligned.

The size of the structure affects segmentation accuracy. Segmentation errors occur on the boundary of surfaces. Thus, the larger the surface of an object, the more voxels on the entire image that can potentially be misclassified. Therefore, accuracy is lower with larger objects than with smaller objects.

Reproducibility was higher with the automated method because only the selection of a few example points is required, not decision making for every voxel on the image during manual segmentation. The reproducibility of brain and tumor segmentation was high. Nevertheless, the inter- and intraobserver reproducibility of both methods was higher with the brain than with the tumor. Larger objects tend to have a volumetric reproducibility that is higher than the overall segmentation accuracy. Because the surface-to-volume ratio behaves approximately like $1/r$ (where r is the object radius), the disagreement about voxel classes on the surface of larger objects with respect to the overall volume is less consequential than it is with smaller objects.

Interobserver variability was substantially reduced with the automated method. Manual interobserver variability was particularly high for low-grade gliomas, which were more difficult to segment, causing deviating expert opinions. Automated segmentation is more robust to expert variation because it involves only the selection of typical example points for training the algorithm, while manual segmentation requires a human decision for every boundary voxel, which is difficult due to, for example, partial voluming. However, intraobserver variability was improved only with meningioma segmentation. For low-grade gliomas, manual intraobserver variability is substantially lower than interobserver variability because the execution of manual segmentation varies, but the opinion regarding the shape of the tumor does not. Therefore, compared with manual segmentation, automated segmentation does not reduce interobserver variability substantially.

Reproducibility was higher with meningiomas with both methods. This findings can be explained by comparing the gray-value distributions of the meningiomas or low-grade gliomas with that of the brain. The meningioma tissue class partially overlaps parts of the skin, the fat in the neck, and the straight and superior sagittal sinuses, and it was well distinguishable from brain tissue with the application of a contrast agent. When the region of interest was restricted to the ICC, the tissue that showed signal intensity overlap with the meningioma was excluded, and the meningioma was successfully segmented.

In some cases of low-grade glioma, the ICC may not have been a sufficient ROI for accurate tumor segmentation due to the similar signal intensities of the tumor and surrounding gray matter. False classifications cannot be corrected if the brain misclassified as tumor tissue is adjacent to the tumor boundary (oversegmentation) or vice versa (undersegmentation). The incorporation of T2-weighted images, which clearly distinguish the tumor as hyperintense tissue, may enable the precise definition of the tumor boundaries. If the voxels of the brain misclassified as tumor are distant to the tumor boundary, if they are connected to the tumor by only thin structures, or if tumor voxels inside the tumor are falsely classified as brain, false classifications can be corrected.

The algorithm developed in this work is based on template-driven segmentation in which an anatomic atlas is used to guide a statistical classification process (8,14,17,18,23). Clark et al (27) proposed a method for automatic detection and segmentation of glioblastoma multiforme on a combination of T1-, T2-, and intermediate-weighted MR images with use of classification and an anatomic knowledge database; accuracy was greater than 90%. Bonnie et al (24) recently reported results with use of an interactive tumor segmentation method. However, its value is difficult to assess because no detail on the segmentation technique is given. Approaches based on MR imaging data alone with use of active contours (25) or multispectral classification (12,13) work well if the tumor shows sufficient contrast to the brain. However, active contours require good initialization, which is difficult to automate, while multispectral classification reveals problems with overlapping intensity distributions.

The lack of automated segmentation methods results in tedious manual labor. This result has been one of the reasons why 3D models have been typically limited to university research settings. The reduction in operator time (3–5 hours to 5–10 minutes) makes it practical to consider the integration of computerized segmentation into daily clinical practice for presurgical 3D planning and intraoperative navigation in routine neurosurgical procedures. A technician carries out the initial work, and a radiologist verifies the result is verified while softreading the images. Our software is currently used on a powerful computer; systems such as ours are becoming increasingly affordable (26).

In conclusion, accurate segmentation is possible for meningiomas and low-grade gliomas with our automated method. Further work is required to extend the tools to a broader range of brain tumors (eg, glioblastoma multiforme). Future clinical studies on the accuracy and reproducibility of our technique in a larger population will be necessary to determine its practical use in a clinical setting.

Appendix

In the following, we give the parameter settings and features used. (For algorithmic details, see references 17 and 18.) The following parameter settings were used: anisotropic diffusion filtering, two iterations; $dt = 0.2$; $\kappa = 5.2$; kNN classification k, 5; number of classes C, five; affine registration, nine degrees of freedom; image resolution levels, three; dis-

tance transform saturation distance, 100; nonlinear registration, three resolution levels; window size w, $9 \times 9 \times 9$; morphologic operators, spherical element; size, $7 \times 7 \times 7$; region growing, connectivity of 18.

Four classification-registration iterations were used for ICC segmentation, one iteration was used for ventricle segmentation, and two iterations were used for tumor segmentation. The brain and ventricle are also resegmented during tumor segmentation.

For segmentation of normal structures (ie, skin, fat, and bone; brain; ventricles), the pattern used in this work was $v_i = [v^1_i, \ldots, v^5_i]^T$, where i is the index to voxel location x_i. The elements v^j_i result from image processing operations T_j as follows: $v^1_i = T_1[I(x_i)]$, where T_1 is anisotropic diffusion filtering ; $v^2_i = T_2[A(x_i)]$, where T_2 is the distance transform of skin, fat, and bone; $v^3_i = T_3[A(x_i)]$, where T_3 is the distance transform of the background of skin, fat, and bone; $v^4_i = T_4[A(x_i)]$, where T_4 is the distance transform of brain; and $v^5_i = T_5[A(x_i)]$, where T_5 is the distance transform of the background of the brain. The elements are applied to the MR image $I(x_i)$ or the image of the registered anatomic atlas $A(x_i)$. While T_1 is carried out only during the preprocessing stage, the operators T_2 to T_5 are applied to the reregistered atlas in every segmentation iteration cycle.

For the first tumor segmentation cycle, the patterns are also $v_i = [v^1_i, \ldots, v^5_i]^T$. For the second tumor segmentation cycle, the patterns are $v_i = [v^1_i, \ldots, v^6_i]^T$, where v^1_i for i = 1–5 are defined as above but with the additional pattern $v^6_i = T_6[A(x_i)]$, T_6: distance transform of initial tumor segmentation where I_b is the resultant image of the first tumor segmentation.

Acknowledgments: The authors thank Rick Schwarz, MD, for helpful comments, and Fatma Ozlen, MD, for help with the manual segmentations.

References

1. Jolesz FA. Image-guided procedures and the operating room of the future. Radiology 1997; 204:601–612.
2. Black PM, Moriarty T, Alexander E, et al. Development and implementation of intraoperative magnetic resonance imaging and its neurosurgical applications. Neurosurgery 1997; 41:831–845.
3. Nakajima S, Atsumi H, Bhalerao AH, et al. Computer-assisted surgical planning for cerebrovascular neurosurgery. Neurosurgery 1997; 41:403–409.
4. Hu X, Tan KK, Levin DN, et al. Three-dimensional magnetic resonance images of the brain: application to neurosurgical planning. J Neurosurg 1990; 72:433–440.
5. Alexander E, Kikinis R, Jolesz FA. Intraoperative magnetic resonance imaging therapy. In: Barnett GH, Roberts D, Guthrie B, eds. Image-guided neurosurgery: clinical applications of interactive surgical navigation. St Louis, Mo: Quality Medical, 1996; 260–266.
6. Kikinis R, Gleason PL, Moriarty TM, et al. Computer assisted interactive three-dimensional planning for neurosurgical procedures. Neurosurgery 1996; 38:640–651.
7. Cline HE, Lorensen E, Kikinis R, Jolesz F. Three-dimensional segmentation of MR images of the head using probability and connectivity. J Comput Assist Tomogr 1990; 14:1037–1045.
8. Vannier MW, Butterfield RL, Rickman DL, Jordan DM, Murphy WA, Biondetti PR. Multispectral magnetic resonance image analysis. Radiology 1985; 154:221–224.
9. Just M, Thelen M. Tissue characterization with T1, T2, and proton-density values: results in 160 patients with brain tumors. Radiology 1988; 169:779–785.
10. Just M, Higer HP, Schwarz M, et al. Tissue characterization of benign tumors: use of NMR-tissue parameters. Magn Reson Imaging 1988; 6:463–472.
11. Gibbs P, Buckley DL, Blackband SJ, Horsman A. Tumor volume determination from MR images by morphological segmentation. Phys Med Biol 1996; 41: 2437–2446.
12. Velthuizen RP, Clarke LP, Phuphanich S, et al. Unsupervised measurement of brain tumor volume on MR images. J Magn Reson Imaging 1995; 5:594–605.
13. Vinitski S, Gonzalez C, Mohamed F, et al. Improved intracranial lesion characterization by tissue segmentation based on a 3D feature map. Magn Reson Med 1997; 37:457–469.
14. Collins DL, Peters TM, Dai W, Evans AC. Model based segmentation of individual brain structures from MRI data. SPIE Vis Biomed Comput 1992; 1808:10–23.
15. Kamber M, Shinghal R, Collins DL, et al. Model-based 3-D segmentation of multiple sclerosis lesions in magnetic resonance brain images. IEEE Trans Med Imaging 1995; 14:442–453.
16. Warfield SK, Dengler J, Zaers J, et al. Automatic identification of gray matter structures from MRI to improve the segmentation of white matter lesions. J Image Guid Surg 1995; 1:326–338.
17. Warfield SK, Kaus MR, Jolesz FA, Kikinis R. Adaptive template moderated spatially varying statistical classification. In: Wells WH, Colchester A, Delp S, eds. Proceedings of the First International Conference on Medical Image Computing and Computer-Assisted Intervention. Boston, Mass: Springer-Verlag, 1998; 431–438.
18. Kaus MR, Warfield SK, Jolesz FA, Kikinis R. Segmentation of meningiomas and low grade gliomas in MRI. In: Taylor C, Colchester A, eds. Proceedings of the Second International Conference on Medical Image Computing and Computer-Assisted Intervention. Cambridge, England: Springer-Verlag, 1999; 1–10.
19. Serra J. Image analysis and mathematical morphology. London, England: London Academic, 1982.
20. Gerig G, Kikinis R, Kubler O, et al. Nonlinear anisotropic filtering of MRI data. IEEE Trans Med Imaging 1992; 11:221–232.
21. Swets A, Pickett RM. Evaluation of diagnostic systems: methods from signal detection theory. Series in Cognition and Perception. New York, NY: Academic Press, 1982.
22. Clarke LP, Velthuizen RP, Phuphanich S, Schellenberg JD, Arrington JA, Silbinger M. MRI: stability of three supervised segmentation techniques. Magn Reson Imaging 1993; 11:95–106.
23. Levin DN, Hu X, Tan KK, et al. The brain: integrated three-dimensional display of MR and PET images. Radiology 1989; 172: 783–789.
24. Bonnie NJ, Fukui MB, Meltzer CC, et al. Brain tumor volume measurement: comparison of manual and semiautomated methods. Radiology 1999; 212:811–816.
25. Zhu H, Francis HY, Lam FK, Poon PWF. Deformable region model for locating the boundary of brain tumors. In: Proceedings of the IEEE 17th Annual Conference on Engineering in Medicine and Biology 1995. Montreal, Quebec, Canada: IEEE, 1995; 411.
26. Kikinis R, Warfield SK, Westin CF. High performance computing (HPC) in medical image analysis (MIA) at the surgical planning laboratory (SPL). In: Proceedings of the Third High Performance Computing Asia Conference and Exhibition. Singapore, Singapore: IEEE; 1998.
27. Clark M. Knowledge guided processing of magnetic resonance images of the brain. Thesis. University of South Florida, Tampa, 1998.